

Simple mineral mapping algorithm based on multitype spectral diagnostic absorption features: a case study at Cuprite, Nevada

Jing Wei,^{a,b,*} Yanfang Ming,^{a,*} Qiang Jia,^c and Dongxu Yang^d

^aShandong University of Science and Technology, Geomatics College, Qingdao, Shandong, China

^bThe Chinese University of Hong Kong, Institute of Space and Earth Information Science, Shatin, New Territories, Hong Kong

^cShandong University of Science and Technology, College of Earth Science and Engineering, Qingdao, Shandong, China

^dZhejiang Tourism College, Xiaoshan, Hangzhou, Zhejiang, China

Abstract. Hyperspectral remote sensing has been widely used in mineral identification using the particularly useful short-wave infrared (SWIR) wavelengths (1.0 to 2.5 μm). Current mineral mapping methods are easily limited by the sensor's radiometric sensitivity and atmospheric effects. Therefore, a simple mineral mapping algorithm (SMMA) based on the combined application with multitype diagnostic SWIR absorption features for hyperspectral data is proposed. A total of nine absorption features are calculated, respectively, from the airborne visible/infrared imaging spectrometer data, the Hyperion hyperspectral data, and the ground reference spectra data collected from the United States Geological Survey (USGS) spectral library. Based on spectral analysis and statistics, a mineral mapping decision-tree model for the Cuprite mining district in Nevada, USA, is constructed. Then, the SMMA algorithm is used to perform mineral mapping experiments. The mineral map from the USGS (USGS map) in the Cuprite area is selected for validation purposes. Results showed that the SMMA algorithm is able to identify most minerals with high coincidence with USGS map results. Compared with Hyperion data (overall accuracy = 74.54%), AVIRIS data showed overall better mineral mapping results (overall accuracy = 94.82%) due to low signal-to-noise ratio and high spatial resolution.

© The Authors. Published by SPIE under a Creative Commons Attribution 3.0 Unported License. Distribution or reproduction of this work in whole or in part requires full attribution of the original publication, including its DOI. [DOI: [10.1117/1.JRS.11.026015](https://doi.org/10.1117/1.JRS.11.026015)]

Keywords: simple mineral mapping algorithm; spectral diagnostic absorption features; Cuprite; airborne visible/infrared imaging spectrometer; Hyperion.

Paper 160980 received Dec. 24, 2016; accepted for publication Apr. 19, 2017; published online May 11, 2017.

1 Introduction

In recent years, due to the continuous bands and high spectral resolutions, hyperspectral remote sensing has been extensively developed in different scientific fields including mineral mapping, disaster or environment monitoring, and vegetation parameter retrieval, among others.^{1–3} Based on the remote sensing technology, mineral information can be efficiently extracted over large spatial scales, which could save considerable manpower and shorten mapping time. Therefore, hyperspectral remote sensing data have been widely applied to mineral exploration.

Traditional mineral mapping methods mainly include spectral matching, unmixing, and local feature matching. Spectral matching is a well-known technology that identifies minerals through the similarity between the spectra obtained from satellite remote sensing data and ground measurements based on different distance functions.^{4,5} Chen et al.⁶ investigated the potential value of some traditional methods, including the spectral angle mapper (SAM) method and the minimum

*Address all correspondence to: Jing Wei, Email: weijing_rs@163.com; Yanfang Ming, E-mail: myf414@163.com

distance method, for geological mapping at Cuprite, Nevada, which showed a good classification performance. Bhattacharya et al.⁷ utilized the SAM method to map altered/weathered and clay minerals over the Dongargarh area based on Hyperion data and collected reference spectra. These methods can achieve a high precision in low vegetation coverage areas, but the spectra can vary significantly due to mixed spectra, atmospheric factors and surface structures, etc.⁸

Spectral unmixing is another standard technology for spectral mixture analysis using a linear or non-linear model. Kruse et al.⁹ used linear spectral unmixing and a knowledge-based expert system to automatically produce mineral maps based on airborne visible/infrared imaging spectrometer (AVIRIS) data in Death Valley, California, and Nevada. Wu and Alan¹⁰ estimated the impervious surface distribution from Landsat ETM+ data using a linear spectral mixture model for spectral mixture analysis and achieved promising accuracy in Columbus. Bioucas et al.¹¹ described geometrical, statistical and spatial-contextual unmixing algorithms as well as mathematical problems and potential solutions. Gonzalez et al.¹² developed a parallel field programmable gate array-based method for spectral unmixing using the image space reconstruction algorithm, which can be used to estimate the abundance of endmembers in hyperspectral images. Spectral unmixing can reduce the mixed spectra effects and has been widely used in complex areas to separate mixed minerals in addition to applications in other fields; however, it mainly relies on the identification of endmembers and spectral differences.¹³

Local spectral feature matching methods usually used unique spectral absorption features embodied in different spectral wavelengths to identify specific mineral types. Commonly used spectral diagnostic absorption features mainly include absorption band position, absorption depth, absorption symmetry, absorption width, etc. For instance, Clark et al.¹⁴ introduced a spectral feature fitting method for spectral matching between targets and reference spectra with specific absorption features. Abílio et al.¹⁵ proposed an analysis of the absorption band positioning method that used the absorption band position to identify alteration minerals. van Ruitenbeek et al.¹⁶ used the diagnostic spectral information of the mineral of interest through band ratios to show predicted wavelengths of white mica in the areas of highest probability. Wei et al.¹⁷ used the optimum index factor to determine the optimal combination of spectral absorption features and performed the mineral mapping experiments with the pattern recognition method using the AVIRIS data in the Cuprite mining district, achieving a high precision. In addition, automatic absorption band methods such as the mapping of asymmetrical shape of absorption bands have been extensively developed and they can achieve high mineral recognition accuracies in single mineral areas.^{18,19} However, spectral absorption features are independently applied to mineral mapping for specific minerals in local areas in early studies.

The above approaches demonstrated that they were influenced by mixed spectra and had difficulty identifying different mineral types in complex regions. Therefore, to improve these methods, a simple mineral mapping algorithm (SMMA) based on the combination of multitype diagnostic spectral absorption features for hyperspectral data is proposed in this paper. Joint application of them can make full use of their adaptability and sensitivity of local spectral changes and can achieve mineral separation with a high precision in local areas with a variety of minerals.

In the current study, two typical hyperspectral data, AVIRIS and Hyperion, of the Cuprite mining district, Nevada, were selected. Multitype spectral absorption features of AVIRIS, Hyperion images, and reference spectra data from the United States Geological Survey (USGS) spectral library were calculated, and the mineral recognition model was built and applied to the Cuprite to perform mineral mapping experiments. Later, the mineral mapping result produced by Clark et al.²⁰ was selected and used to verify the experimental results.

2 Study Area

The Cuprite mining district is located on the border of Esmeralda and Nye counties in southwestern Nevada, USA (37°28' to 37°40' N, 117°8' to 117°20' W) (Fig. 1). The elevation of Cuprite ranges from 1420 to 1700 m above sea level. Cuprite has abundant mineral resources,



Fig. 1 Geographical location of Cuprite mining district, Nevada, USA.

with a wide variety of rock types exposed and sparse vegetation coverage (<15%) that includes sheep grass, juniper, small cacti, and sagebrush. It is separated into two regions by highway US-95. Cambrian metasedimentary rocks cover most of the western part of the Cuprite area.^{21,22} The oldest Cambrian unit contains abundant muscovite, which exhibits an Al-OH 2.2- μm absorption feature, and calcite, which typically exhibits a (CO_3) 2.33- μm spectral absorption feature.²³ The Tertiary volcanic rocks cover the central and eastern parts of the study area and are divided into three parts, i.e., the argillaceous alteration belt, the silicified alteration belt, and the opal alteration zone.^{21,22} The argillaceous alteration belt primarily consists of alunite, dickite, and kaolinite, which exhibits doublet absorption features at 2.17 and 2.2 μm . The silicic area forms a large irregular patch extending from the middle to the south of Cuprite, including quartz. The opal alteration belt mainly contains opal. Silicified and opalized rocks have a broad absorption feature centred at 2.26 μm .²¹⁻²³ As a typical well-understood mineralogical area, a wide range of research has been conducted, leading to extensive mineral mapping.^{8-10,21,24-27}

3 Data Sets and Processing

3.1 Data Sets

In this paper, ground measured reference spectra data and two sets of hyperspectral data are employed. The ground measured spectra data were collected from the USGS spectral library, and the hyperspectral data consist of AVIRIS and Hyperion data. The USGS spectral library is oriented to mineral resources exploration based on the combination of the JPL standard spectra database, released in September 2007. The spectra data are collected using a Beckman 5270 spectrometer, including 481 examples of typical minerals. Each mineral spectrum covers the spectral range of 0.2 to 3.0 μm with a spectral resolution of 10 nm. Seven types of typical minerals, alunite, kaolinite, montmorillonite, muscovite, calcite, and chlorite, are selected in this paper to perform mineral mapping experiments in the Cuprite mining district.

AVIRIS is jointly developed by the American space agency NASA and Jet Propulsion Laboratory (JPL) and has been flown since 1987. The AVIRIS sensor acquires data in the spectral range of 0.4 to 2.5 μm for a total of 224 spectral bands at a spectral resolution of 10 nm and a spatial resolution of 3 to 15 m. NASA's Earth Observing-1 (EO-1) Hyperion sensor has been in continuous operation since November 2000. Hyperion data cover a spectral range of 0.4 to 2.5 μm , with a spectral resolution of 10 nm and a spatial resolution of ~30 m from a 705-km orbit, for a total of 242 spectral bands.²⁸ The data are calibrated to radiance using both premission and on-orbit measurements. Table 1 shows a comparison of key features between AVIRIS and Hyperion data.

Table 1 Comparison of key features between AVIRIS and Hyperion data.

Features	AVIRIS	Hyperion
Wavelength range (μm)	0.4 to 2.5	0.4 to 2.5
Number of channels	224	242
Spectral resolution (nm)	10	10
Spatial resolution (m)	3 to 15	30
Swath width (km)	10.5	7.5
SWIR SNR	~500:1	~50:1

3.2 Data Processing

For reference spectra data from the USGS spectral library, spectral resampling is required to match the other hyperspectral data with different spectral resolutions. Spectral resampling is usually based on a Gaussian function and uses the centre wavelength of full width of half maximum spectral response in an imaging spectrometer,

$$\rho' = \sum_{\lambda=1}^N [\beta(\lambda) \times \rho(\lambda)] / \sum_{\lambda=1}^N \beta(\lambda), \quad (1)$$

where ρ' is the resampling spectra, $\rho(\lambda)$ is the origin spectra, and $\beta(\lambda)$ is the weight of spectral response function of each channel for different hyperspectral images.

For AVIRIS data, image processing mainly includes the invalid bands removal, radiometric calibration, and atmospheric correction. Due to poor data quality, data processing required for the Hyperion data mainly includes bad line and invalid band removal, atmospheric correction, stripe removal, and spectra smoothing. Bad lines are removed using the neighbourhood averaging method. Invalid spectral bands affected by atmospheric water absorption as well as low signal-to-noise ratio (SNR) are removed (bands 1 to 2, 105 to 115, 150 to 170, and 223 to 224 of AVIRIS, bands 77 to 78 of Hyperion). For Hyperion data, some bands without radiation calibration should also be removed (bands 1 to 7, 58 to 76, and 225 to 242). In this study, 36 bands of AVIRIS data and 87 bands of Hyperion data are removed.

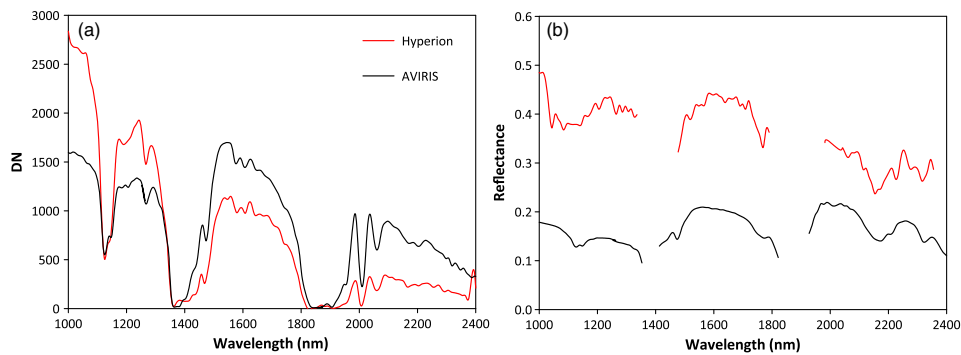
To obtain land surface reflectance, atmospheric correction is necessary for both AVIRIS and Hyperion data. In this paper, AVIRIS and Hyperion data were both converted to surface reflectance using the fast line-of-sight atmospheric analysis of hypercubes (FLAASH) model provided by the environment for visualizing images software. The FLAASH model is a type of atmospheric correction method that is based on moderate resolution atmospheric transmission (MODTRAN4) radiative transfer mode,²⁹ suitable for different types of sensors. Table 2 provides the main atmospheric correction parameters for both AVIRIS and Hyperion images. Figure 2 shows alunite spectra before and after atmospheric correction.

There are two obvious water vapor absorption bands approximately at 1350 to 1450 nm and 1800 to 1950 nm. However, most certainly alteration minerals have distinctive and unique absorption features in the short-wave infrared (SWIR) range of 1900 to 2500 nm. In this paper, considering the selected typical minerals spectra, 2000 to 2500 nm of AVIRIS, total of 50 spectral bands, and the 1980 to 2400 nm of Hyperion, total of 35 bands are selected for mineral mapping experiments.

There are different degrees of regular stripes appearing in most bands of Hyperion data due to the Earth's inherent features and inherent noise. In this paper, the global stripe method is selected to remove stripes,^{30,31} which can better improve the image quality and retain the original spectral information. Moreover, hyperspectral data are often affected by noise, and abundant researches have been conducted on noise filtering.³² The hamming window filter is selected in this study to smooth the spectra in order to reduce the noise influence for Hyperion data.^{33,34}

Table 2 Main atmospheric correction parameters used in FLAASH models.

Sensor type	AVIRIS	Hyperion
Scene center location	Metadata	Metadata
Sensor altitude (km)	20	705
Ground elevation (km)	DEM	DEM
Pixel size (m)	3 to 15	30
Fight date and time GMT	Metadata	Metadata
Atmospheric model	Midlatitude summer/winter	Midlatitude summer/winter
Aerosol model	Rural	Rural
Aerosol retrieval	2-band (K-T)	2-band (K-T)
Water retrieval	Yes	Yes
Water absorption feature	1135 nm	1135 nm
Initial visibility (km)	0 to 40	0 to 40
Other parameters	Default values	Default values

**Fig. 2** Alunite spectra (a) before and (b) after atmospheric correction.

4 Methodology

4.1 Diagnostic Spectral Absorption Features Extraction

The diagnostic spectral absorption features used in this paper mainly include absorption band position (P), absorption reflectance (R_p), absorption width (W), absorption symmetry (S), absorption depth (H), absorption area (A), spectral absorption index (SAI), etc. They can be extracted through the continuum removed reflectance spectra.

Continuum removal is a common spectral enhancement technology for hyperspectral data, which can highlight the spectral absorption and reflection features effectively. With continuum removal, absorption features were normalized to the same spectral features background, and the absorption features can be extracted and applied to identify mineral types. The continuum-removed spectrum is calculated by dividing the original reflectance values within the spectral feature by the corresponding values of a continuum line established between the two endpoints of the feature.^{35,36} Figure 3 shows detailed definitions of different spectral absorption features. Each absorption feature is composed of the spectral absorption valley point and two shoulders.^{37,38}

The absorption band position is located at the point P , which has the minimum spectral reflectance. The absorption reflectance (R_p) refers to the corresponding reflectance of P .

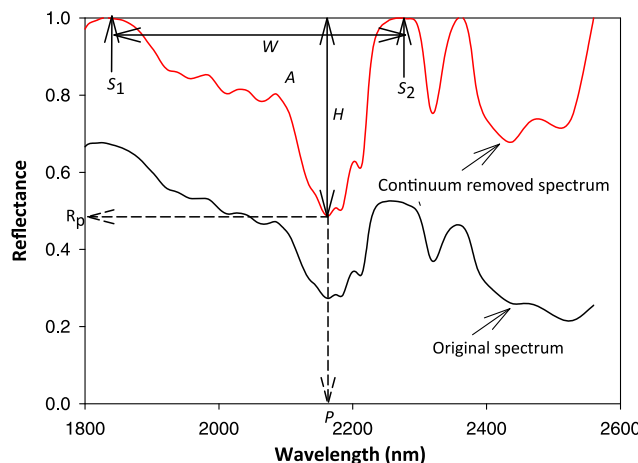


Fig. 3 Definition of multitype spectral diagnostic absorption features.

The absorption width (W) is the difference in wavelengths between the two shoulders (S_1 and S_2) of point P [Eq. (2)] and the spectral absorption symmetry (S) can be defined as Eq. (3). The spectral absorption depth (H) is defined as the distance between R_p and 1 [Eq. (4)]. The spectral absorption area (A) refers to the triangle area composed of the points R_p and two absorption shoulders [Eq. (5)]. The band position of P is selected first as the initial value, then gradually decreases (increases) from P toward the left (right) side until it first meets the Eq. (6). The values on the left and right sides, respectively, represent the left (S_1) and right (S_2) absorption shoulder positions. The SAI is defined as the reciprocal of the ratio between the reflectance of point P and the corresponding value of the spectral absorption baseline [Eq. (7)]

$$W = \lambda_2 - \lambda_1, \quad (2)$$

$$S = (\lambda_1 - \lambda_P)/W, \quad (3)$$

$$H = 1 - R_p, \quad (4)$$

$$A = H * W/2, \quad (5)$$

$$|1 - \rho| = 0, \quad (6)$$

$$\text{SAI} = [S * R_1 + (1 - S) * R_2]/R_p, \quad (7)$$

where λ_1, λ_2 are the wavelength and R_1, R_2 are the reflectances of left (S_1) right (S_2) shoulder positions for point P , λ_p is the wavelength of point P , ρ is the reflectance. In this study, a total of nine spectral absorption feature parameters are calculated for AVIRIS, Hyperion, and reference spectra from the USGS spectral library, respectively.

4.2 Simple Mineral Mapping Algorithm

4.2.1 Spectral analysis

Figure 4 shows the typical mineral spectra of the spectral ranges from 2000 to 2500 nm after continuum removal. Three types of clay minerals, kaolinite, montmorillonite, and chlorite, show relatively complex spectra. Kaolinite shows a strong double absorption approximately at 2180 and 2210 nm, and montmorillonite has a close absorption feature distributed around

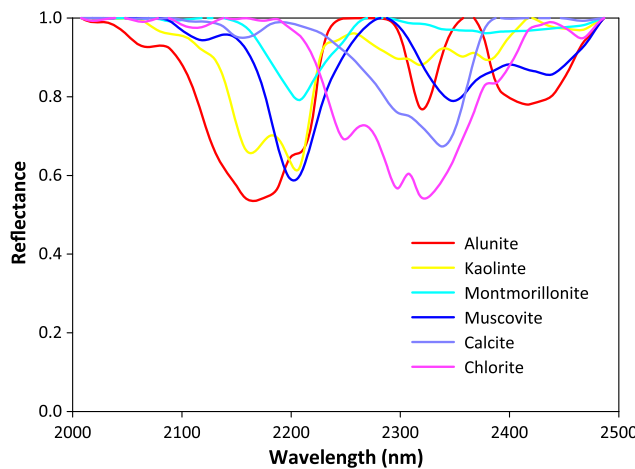


Fig. 4 Continuum removed spectra of typical minerals in Cuprite.

2220 nm. The absorption feature of chlorite is approximately at 2320 nm. Muscovite is part of the phyllosilicate group with a strong absorption feature approximately at 2200 nm and a large absorption symmetry. Calcite, a type of carbonate mineral, has a close absorption feature distributed at 2330 to 2340 nm, showing a greater difference from the other minerals. Alunite is characterized by absorption features due to the OH frequency stretching at 2150 to 2170 nm, and an approximately symmetrical shape at 2100 to 2250 nm, with a second broad absorption at 2320 nm, and a third broad absorption at 2420 nm. However, a vibrational absorption feature at 2160 nm is the main diagnostic spectral absorption feature distinguishing alunite from other clay minerals, as well as the lower absorption reflectance.

4.2.2 Decision-tree rules generation

Based on the spectral analysis, the mineral mapping accuracy can be improved by using a variety of spectral absorption features. Table 3 shows distribution ranges of multitype spectral absorption features of different mineral types calculated from the USGS spectral library.

It is observed that different minerals show different distribution ranges on certain spectral absorption features. Alunite has an absorption position (P) approximately at 2166 nm, with a low absorption reflectance ($R < 0.65$), SAI, and small left absorption shoulder position (S_1) less than 10, respectively. Kaolinite has a similar $P \sim 2208$ nm with montmorillonite ($P \sim 2212$ nm) and muscovite ($P \sim 2203$ nm), but a stable absorption width (W) ranging from 350 to 380 and a smaller S_1 than alunite. However, montmorillonite has a wide W range ($W \sim 90$ to 250) and a high reflectance ($R > 0.70$). It also has a small absorption depth (H) and absorption area (A) less than 0.30 and 20, respectively. Muscovite has a relatively wider range of $A \sim 20$ to 50 and absorption symmetry ($S \sim 0.3$ to 0.8) than other minerals. Calcite and chlorite show similar absorption positions approximately at 2337 and 2324 nm, whereas calcite has a stable W ranging from 280 to 310 and a smaller right absorption shoulder position ($S_2 < 40$) than chlorite. According to the above analysis, a decision-tree model of mineral recognition is constructed as

- Alunite: $P \in (2158, 2168)$ and $W \in (200, 250)$ and $R < 0.65$ and $SAI < 0$ and $S_1 < 10$,
- Kaolite: $P \in (2200, 2210)$ and $W \in (350, 380)$ and $S_1 < 10$,
- Muscovite: $P \in (2190, 2210)$ and $A \in (20, 50)$ and $S \in (0.3, 0.8)$,
- Kaolite + Muscovite: $P \in (2190, 2210)$ and $W \in (280, 360)$ and $S > 030$ and $S_1 < 10$,
- Montmorillonite: $P \in (2200, 2220)$ and $W \in (90, 250)$ and $R > 0.70$ and $H < 0.30$ and $A < 20$,
- Calcite: $P \in (2330, 2340)$ and $W \in (280, 310)$ and $S < 0.25$ and $S_2 \in (30, 40)$,
- Chlorite: $P \in (2310, 2330)$ and $S_2 > 40$.

Table 3 Distribution ranges of multitype spectral absorption features.

	P			R			W		
	Min	Max	Mean	Min	Max	Mean	Min	Max	Mean
Alunite	2158	2168	2166	0.28	0.66	0.53	209.89	249.98	236.65
Kaolinite	2208	2208	2208	0.58	0.69	0.65	359.18	379.23	367.20
Montmorillonite	2207	2217	2212	0.74	0.97	0.80	99.82	239.24	147.01
Muscovite	2197	2207	2203	0.59	0.80	0.69	199.78	408.65	260.44
Kao+Mus	2197	2208	2203	0.58	0.75	0.67	280.32	360.23	312.62
Calcite	2337	2337	2337	0.67	0.73	0.70	289.24	309.26	299.28
Chlorite	2317	2327	2324	0.55	0.80	0.66	239.12	328.61	278.87
	H			A			S		
	Min	Max	Mean	Min	Max	Mean	Min	Max	Mean
Alunite	0.21	0.72	0.43	22.26	82.53	51.24	0.37	0.48	0.40
Kaolinite	0.31	0.42	0.35	33.05	68.07	53.36	0.25	0.58	0.46
Montmorillonite	0.03	0.26	0.20	2.99	20.16	13.70	0.27	0.62	0.49
Muscovite	0.20	0.41	0.31	21.85	48.05	35.03	0.38	0.79	0.53
Kao+Mus	0.15	0.41	0.34	23.45	54.26	40.02	0.30	0.64	0.48
Calcite	0.27	0.33	0.30	39.34	48.80	45.13	0.17	0.21	0.19
Chlorite	0.20	0.45	0.34	23.78	74.05	48.47	0.36	0.59	0.45
	SAI			S_1			S_2		
	Min	Max	Mean	Min	Max	Mean	Min	Max	Mean
Alunite	-11.34	-1.33	-3.78	1	5	1	24	26	25
Kaolinite	1.44	1.72	1.54	3	6	5	25	41	35
Montmorillonite	1.03	1.35	1.26	5	16	13	26	39	28
Muscovite	1.25	1.68	1.46	5	14	9	27	48	33
Kao+Mus	1.32	1.70	1.51	5	8	7	28	44	34
Calcite	1.37	1.48	1.43	8	10	9	38	39	39
Chlorite	1.25	1.82	1.53	14	21	17	41	48	45

5 Results and Discussion

5.1 Mineral Mapping Experiments

The mineral recognition model is applied to five AVIRIS images and two Hyperion images in the Cuprite mining district. A total of seven types of minerals, alunite, kaolinite, montmorillonite, muscovite, calcite, chlorite, and a mixture of kaolinite and muscovite, are identified in Cuprite mining district using the SMMA algorithm. Figure 5 shows the mineral mapping results.

Figure 6 shows the common region of mineral mapping results in the Cuprite from AVIRIS and Hyperion data. It is observed that the mineral recognition model can adequately identify

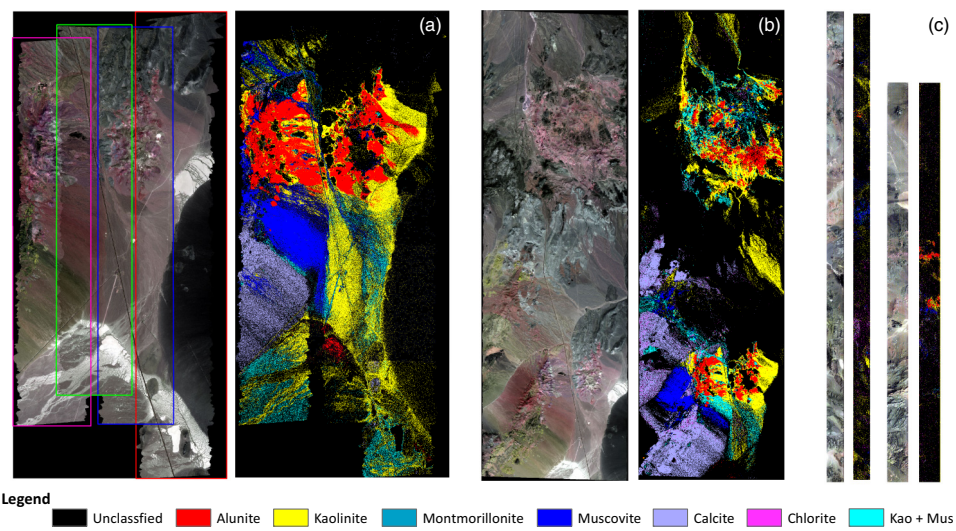


Fig. 5 (Left) False color synthesis images and (right) corresponding mineral mapping results in Nevada, USA of (a) f060502t01p00r04, f060502t01p00r05, f060502t01p00r06, and f060502t01p00r07, AVIRIS; (b) f060920t01p00r05, AVIRIS; (c) E01H0410342001204111P1 and E01H0410342011037110KF, Hyperion.

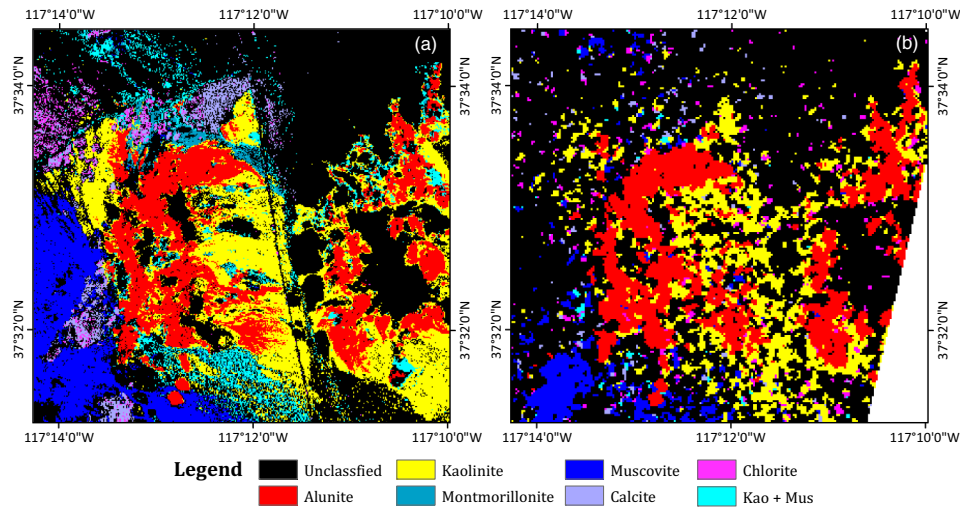


Fig. 6 Common mineral mapping results in Cuprite for (a) AVIRIS and (b) Hyperion images.

most minerals in Cuprite. Mineral mapping results showed that the west area of Cuprite mainly includes alunite, kaolinite, montmorillonite, muscovite, and a certain amount of calcite and chlorite. The east area mainly contains alunite, kaolinite, and a small amount of montmorillonite. Alunite, kaolinite, and muscovite are widely distributed and concentrated in Cuprite, yet the montmorillonite, calcite, and chlorite are overall small and fragmented. Visual comparisons indicate that AVIRIS can identify similar types of minerals and produce similar mineral mapping results as Hyperion; however, Hyperion shows overall worse mapping results than AVIRIS.

5.2 Mineral Mapping Accuracy Assessment

For comparative purposes, a mineral map produced by the USGS library (USGS map)^{20,39} is selected in this paper, which is used to map different minerals presented in Cuprite (Fig. 7). This USGS map is generated using the USGS tricorder algorithm with technologies of waveform matching, least square fitting, and diffraction analysis based on AVIRIS data. Moreover, it is

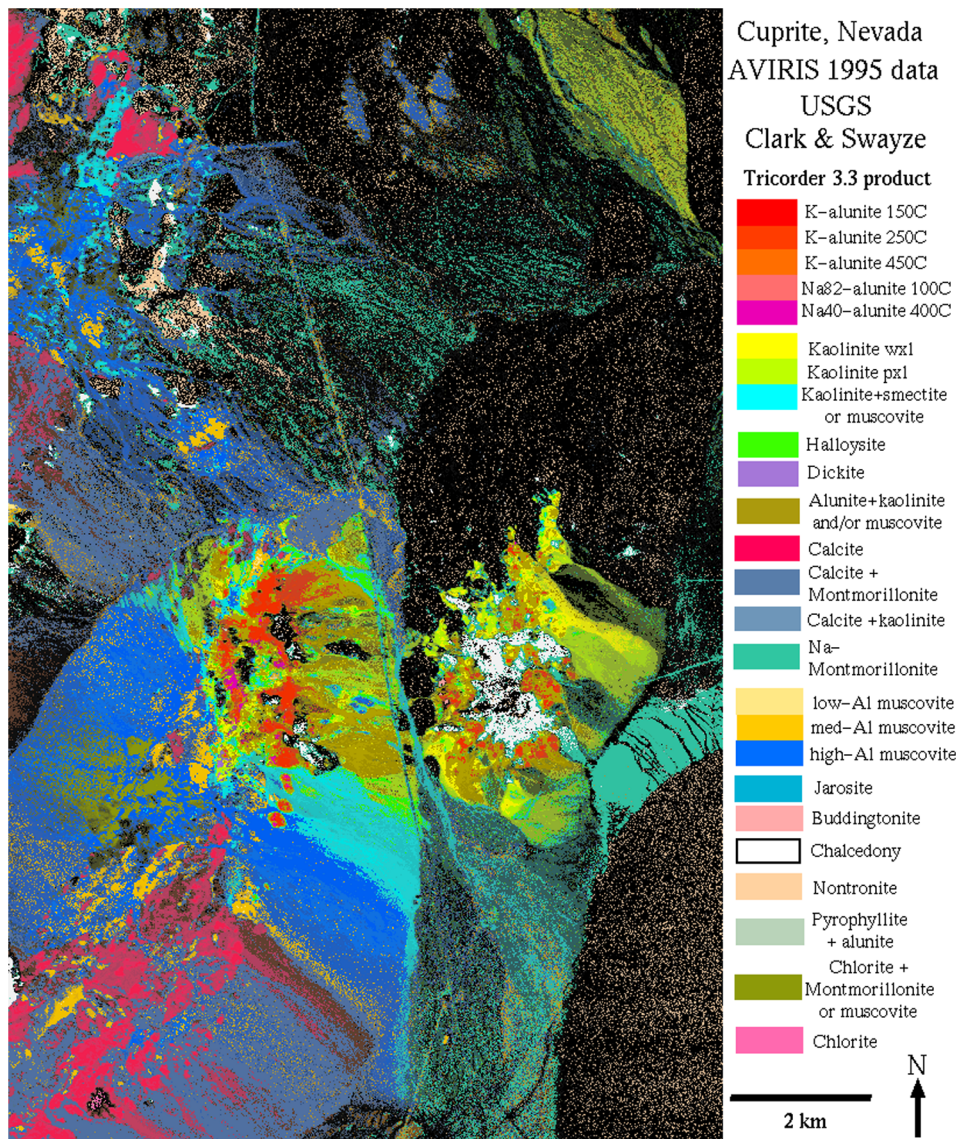


Fig. 7 USGS map of the location of different minerals in the Cuprite mining district. The map is available online at http://speclab.cr.usgs.gov/cuprite95.tif.2.2um_map.gif.

verified with field investigation combined with ground-measured data and shows an overall high accuracy compared with ground observations. It serves as a good indicator for qualitative and quantitative assessments of mineral mapping and has been widely applied to validations of Cuprite mineral recognition results. First, the geometric correction of the USGS mineral map was conducted by selecting control points and then, the minerals were extracted and merged into seven types in order to match the mineral mapping results in this paper.

For qualitative comparison, several typical minerals, alunite, kaolinite, and muscovite, were extracted from USGS map, AVIRIS, and Hyperion mapping results, respectively. Figure 8 shows the qualitative comparison between the mineral mapping results and the USGS map in Cuprite. It is clear to see that alunite, kaolinite, and muscovite were effectively identified in both AVIRIS and Hyperion images. They showed a strong alignment with the USGS map. However, compared with Hyperion, the three typical minerals, especially for kaolinite, and muscovite can be better identified in the AVIRIS data.

For quantitative evaluation, the Kappa coefficient (K) with the overall and user's accuracies are computed for a measure of how well the mineral mapping result agrees with the USGS map. Each mineral was extracted independently from the USGS map as the validation samples to match with the experiment results. Table 4 shows the mineral mapping accuracies of AVIRIS and Hyperion data.

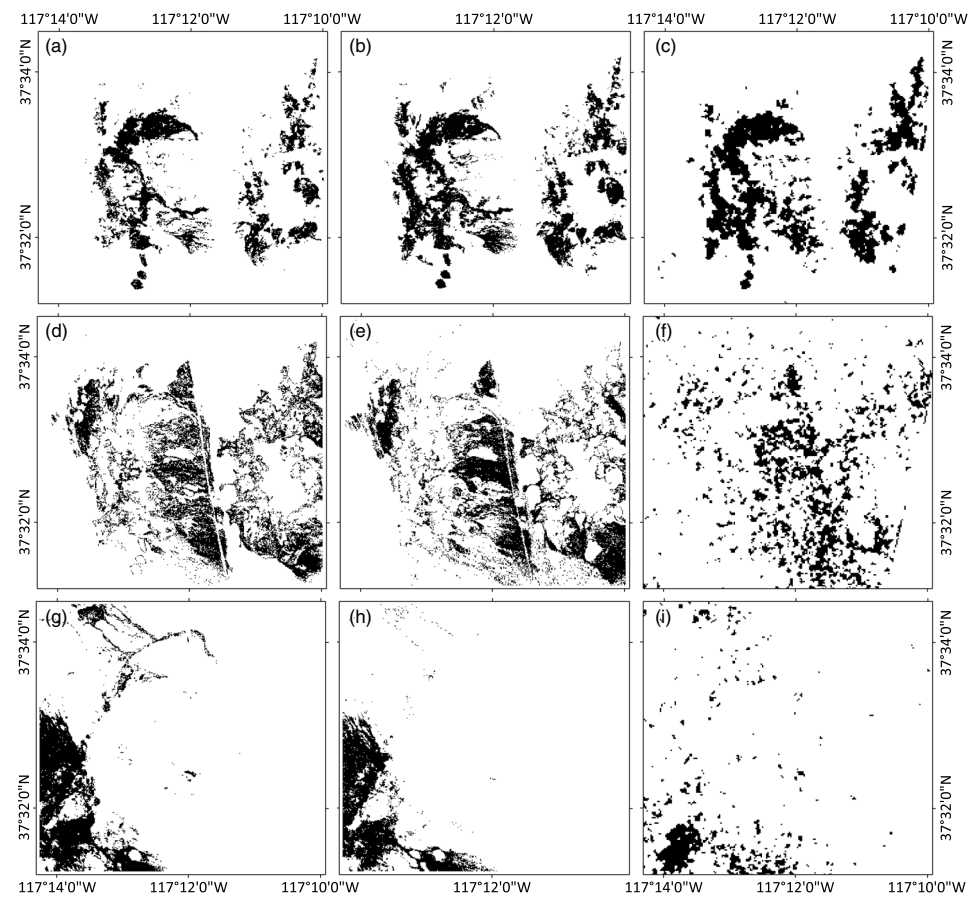


Fig. 8 Qualitative comparisons among different mineral mapping results in Cuprite, Nevada. (a)–(c) The alunite; (d)–(f) the kaolinite; (g)–(i) the muscovite from USGS map, AVIRIS, and Hyperion data, respectively.

Table 4 Accuracy statistics of the mineral mapping results.

Matrix	Accuracy (%)			
	AVIRIS		Hyperion	
	Prod. acc. (%)	User acc (%)	Prod. acc. (%)	User acc (%)
Alunite	95.08	97.94	92.22	82.56
Kaolinite	94.79	91.84	67.05	68.37
Montmorillonite	58.59	65.82	12.36	59.81
Muscovite	96.37	99.74	81.25	88.91
Calcite	86.07	76.00	54.46	36.18
Chlorite	71.03	51.58	68.48	14.16
Kao + Mus	97.57	94.25	—	—
Kappa	0.9317		0.6234	
Prod. acc. (%)	94.82		74.54	

The mineral mapping result of AVIRIS data exhibited a strong accuracy with the USGS map. The overall accuracy reached 94.82% with a Kappa coefficient of 0.9317. The SMMA algorithm can identify seven types of minerals with a contact ratio above 65% for most minerals. The mixture of kaolinite and muscovite, muscovite, alunite, and kaolinite showed overall good recognition results, with high producer's accuracies of 97.57%, 96.37%, 95.08%, and 94.79%, respectively. However, chlorite and montmorillonite showed overall low recognition accuracies with low agreements of 71.03% and 58.59% compared with the USGS map.

The mineral mapping result of Hyperion data agreed well with the USGS map but showed an overall worse accuracy than AVIRIS data. This method was able to identify seven types of minerals for Hyperion with an overall accuracy of 74.54% and a Kappa coefficient of 0.6234 (Table 4). Alunite, muscovite, chlorite, and kaolinite showed high consistencies with the USGS map, with producer's accuracy of 92.22%, 81.25%, 68.48%, and 67.05%, respectively. Calcite and montmorillonite showed overall low accuracies of 54.46% and 12.36%.

From the above analysis, AVIRIS data can identify similar typical minerals with that of Hyperion data, but Hyperion data showed an overall lower mineral mapping accuracy than that of AVIRIS data. The main reason was the low SNRs of the Hyperion data. However, to some extent, the difference in pixel size was still causing some loss of spatial detail in the Hyperion mineral mapping result. Additionally, AVIRIS data showed a basic mineral mapping result of which it was possible to obtain more detailed mineral information. However, mineral recognition by Hyperion was possible and actually Hyperion demonstrated a relatively good mapping result considering the overall SNRs of the SWIR channels after the rigorous data processing.

Alunite, kaolinite, and muscovite showed high recognition accuracy in accordance with the USGS map in two hyperspectral datasets. The main reason is that these minerals are widely and intensively distributed, and the spectral absorption features were obvious and easily identified. However, calcite, chlorite, and montmorillonite showed overall low accuracies in both AVIRIS and Hyperion data. The main reason is that these minerals are distributed more dispersedly and are easily affected by surrounding derived minerals. In addition, montmorillonite always presents in mixtures,^{39,40} adding the identification difficulties. Within the adjoining pixel, due to the effects of data noise in the hyperspectral data, some scattered pixels at the edge were divided into minerals, resulting in a relatively low accuracy.

6 Conclusions

A mineral recognition decision-tree model of this paper is developed based on the analysis of multitype diagnostic spectral absorption features. The types and scopes of thresholds for the spectral absorption features corresponding to different mineral types are determined, and an SMMA with the combined application of multitype spectral absorption features is proposed and applied to mineral mapping experiments from airborne/satellite hyperspectral images of AVIRIS and Hyperion. Finally, the mineral map produced by the USGS library is selected to verify the experiment results. Validation results show that the SMMA can identify most minerals in Cuprite and the experiment results show overall high consistency with the USGS map. Both AVIRIS and Hyperion data show similar mineral mapping results and different mineral types show certain differences in recognition precision; however, due to effects of low SNR, spatial resolution, and other factors, Hyperion shows a relatively worse mineral mapping result ($K = 0.6234$, overall accuracy = 74.54%) than that of AVIRIS ($K = 0.9317$, overall accuracy = 94.82%).

Although the proposed algorithm is suitable and obtains high accuracies, this work is limited by some shortcomings of the decision-tree classification method. This method requires high precision of data processing which is easily affected by image noise; results of the information gain are biased to a category with more numerical features; it ignores correlations among different attributes. Future work will focus on exploring the relevant relationship among the multitype spectral absorption parameters, mineral abundance and element content, and the contribution evaluation method of different minerals in the combined application of multitype spectral absorption parameters.

Acknowledgments

The authors also thank NASA and JPL for providing the Hyperion and AVIRIS data, and the mineral map in Cuprite produced by Clark and Swayze. The authors are thankful for the support of the National Key Technology Support Program (No. 2012BAH27B04), the Outstanding Youth Fund of Shandong Province (No. JQ201211), the Graduate Innovation Fund of Shandong University of Science and Technology (No. SDKDYC170103), the International Cooperation Project of Zhejiang Science and Technology Department (No. 2016C34003), and the Public Welfare Technology Research Social Development Project of Zhejiang Science and Technology Department (No. 2013C33042).

References

1. F. H. Goetz et al., "Imaging spectrometry for earth remote sensing," *Science* **228**, 1147–1153 (1985).
2. C.-I. Chang, *Hyperspectral Imaging: Techniques for Spectral Detection and Classification*, Springer, New York (2007).
3. A. Linear, "Foreword to the special issue on spectral unmixing of remotely sensed data," *IEEE Trans. Geosci. Remote Sens.* **49**(11), 4103–4110 (2011).
4. F. A. Kruse, J. W. Boardman, and J. F. Huntington, "Comparison of airborne hyperspectral data and EO-1 Hyperion for mineral mapping," *IEEE Trans. Geosci. Remote Sens.* **41**(6), 1388–1400 (2003).
5. S. A. Robila, "Using spectral distance for speed up in hyperspectral image processing," *Int. J. Remote Sens.* **26**(24), 5629–5650 (2005).
6. X. F. Chen, T. A. Warner, and D. J. Campagna, "Integrating visible, near-infrared and short-wave infrared hyperspectral and multispectral thermal imagery for geological mapping at Cuprite, Nevada," *Remote Sens. Environ.* **110**, 344–356 (2007).
7. S. Bhattacharya et al., "Utilization of Hyperion data over Dongargarh, India, for mapping altered/weathered and clay minerals along with field spectral measurements," *Int. J. Remote Sens.* **33**(17), 5438–5450 (2012).
8. D. R. Thompson et al., "Autonomous spectral discovery and mapping onboard the EO-1 spacecraft," *IEEE Trans. Geosci. Remote Sens.* **51**(6), 3567–3579 (2013).
9. F. A. Kruse, A. B. Lefkoff, and J. B. Dietz, "Expert system-based mineral mapping in northern Death Valley, California/Nevada using the airborne visible/infrared imaging spectrometer (AVIRIS)," *Remote Sens. Environ.* **44**, 309–336 (1993).
10. C. S. Wu and T. M. Alan, "Estimating impervious surface distribution by spectral mixture analysis," *Remote Sens. Environ.* **84**, 493–505 (2003).
11. J. Bioucas et al., "Hyperspectral unmixing overview: geometrical, statistical, and sparse regression-based approaches," *IEEE J. Sel. Top. Appl. Earth Obs. Remote Sens.* **5**(2), 354–379 (2012).
12. C. González et al., "FPGA implementation of abundance estimation for spectral unmixing of hyperspectral data using the image space reconstruction algorithm," *IEEE J. Sel. Top. Appl. Earth Obs. Remote Sens.* **5**(1), 248–261 (2012).
13. S. Bernabe et al., "Hyperspectral unmixing on GPUs and multi-core processors: a comparison," *IEEE J. Sel. Top. Appl. Earth Obs. Remote Sens.* **6**(3), 1386–1398 (2013).
14. R. N. Clark, A. J. Gallagher, and G. A. Swayze, "Material absorption band depth mapping of imaging spectrometer data using a complete band shape least-squares fit with library reference spectra," in *Proc. of 1990 the Second Airborne Visible/Infrared Imaging Spectrometer (AVIRIS) Workshop*, Denver, Colorado, pp. 4–5 (1990).
15. O. Abílio et al., "Analysis absorption band positioning: a new method for hyperspectral image treatment," in *Proc. of 2001 AVIRIS Workshops*, Pasadena, California, pp. 59–65 (2001).
16. F. J. A. van Ruitenbeek et al., "Mapping white micas and their absorption wavelengths using hyperspectral band ratios," *Remote Sens. Environ.* **102**, 211–222 (2006).
17. J. Wei, Y. Ming, and F. Liu, "Hyperspectral mineral mapping method based on spectral characteristic parameter combination," *Earth Sci.* **40**(8), 1432–1440 (2015).

18. A. J. Brown, "Spectral curve fitting for automatic hyperspectral data analysis," *IEEE Trans. Geosci. Remote Sens.* **44**(6), 1601–1608 (2006).
19. A. J. Brown et al., "Hydrothermal formation of clay-carbonate alteration assemblages in the Nili Fossae region of Mars," *Earth Planet. Sci. Lett.* **297**, 174–182 (2010).
20. R. N. Clark and G. A. Swayze, "Mapping minerals, amorphous materials, environmental materials, vegetation, water, ice and snow, and other materials: the USGS tricorder algorithm," in *Summaries of the Fifth Annual JPL Airborne Earth Sciences Workshop*, Vol. 1, pp. 39–40, JPL Publication 95-1, Pasadena, California (1995).
21. R. P. Ashley and M. J. Abrams, "Alteration mapping using multispectral images; cuprite mining district esmeralda county, nevada," *Appl. Environ. Microbiol.* **39**(1), 261 (1980).
22. G. A. Swayze, "The hydrothermal and structural history of the Cuprite Mining District, southwestern Nevada: an integrated geological and geophysical approach," PhD Dissertation, pp. 6–117, University of Colorado, Boulder (1997).
23. J. C. Mars and L. C. Rowan, "Spectral assessment of new aster SWIR surface reflectance data products for spectroscopic mapping of rocks and minerals," *Remote Sens. Environ.* **114**(9), 2011–2025 (2010).
24. D. R. Thompson et al., "Autonomous spectral discovery and mapping onboard the EO-1 spacecraft," *IEEE Trans. Geosci. Remote Sens.* **51**(6), 1–13 (2012).
25. F. A. Kruse, K. S. Kierein-Young, and J. W. Boardman, "Mineral mapping at Cuprite, Nevada with a 63-channel imaging spectrometer," *Photogramm. Eng. Remote Sens.* **56**(1), 83–92 (1990).
26. S. J. Hook et al., "A comparison of techniques for extracting emissivity information from thermal infrared data for geologic studies," *Remote Sens. Environ.* **42**(2), 123–135 (1992).
27. M. D. Iordache, J. M. Bioucas-Dias, and A. Plaza, "Collaborative sparse regression for hyperspectral unmixing," *IEEE Trans. Geosci. Remote Sens.* **52**(1), 341–354 (2014).
28. J. Pearlman et al., "Overview of the Hyperion imaging spectrometer for the NASA EO-1 mission," in *Proc. of the Int. Geoscience and Remote Sensing Symp. (IGARSS '01)*, Vol. 7, pp. 3036–3038 (2001).
29. G. W. Felde et al., "Analysis of Hyperion data with the FLAASH atmospheric correction algorithm," in *Proc. of the Int. Geoscience and Remote Sensing Symp. (IGARSS '03)*, Toulouse, France, pp. 90–92, IEEE, Piscataway, New Jersey (2003).
30. G. Corsin, M. Diani, and T. Walze, "Striping removal in MOS-B data," *IEEE Trans. Geosci. Remote Sens.* **38**(3), 1439–1446 (2000).
31. N. Acit, M. Diani, and G. Corsini, "Subspace-based striping noise reduction in hyperspectral images," *IEEE Trans. Geosci. Remote Sens.* **49**(4), 1325–1342 (2011).
32. S. G. Lenio, R. F. Antonio, and A. T. Daniela, "Discrimination of sugarcane varieties in Southeastern Brazil with EO-1 Hyperion data," *Remote Sens. Environ.* **94**(4), 523–534 (2005).
33. L. D. Enochson and R. K. Otnes, *Programming and Analysis for Digital Time Series Data*, p. 142, U.S. Department of Defense, Shock and Vibration Information Center (1968).
34. A. H. Nuttall, "Some windows with very good sidelobe behavior," *IEEE Trans. Acoust. Speech Signal Process.* **29**(1), 84–91 (1981).
35. Z. Huang et al., "Estimating foliage nitrogen concentration form HYMAP data using continuum removal analysis," *Remote Sens. Environ.* **93**, 18–29 (2004).
36. I. D. Sanches, C. R. S. Filho, and R. F. Kokaly, "Spectroscopic remote sensing of plant stress at leaf and canopy levels using the chlorophyll 680 nm absorption feature with continuum removal," *ISPRS J. Photogramm. Remote Sens.* **97**, 111–122 (2014).
37. F. A. Kruse, G. L. Raines, and K. Watson, "Analytical techniques for extracting geologic information from multichannel airborne spectroradiometer airborne imaging spectrometer data," in *Proc. of the Fourth Thematic Conf. on Geologic Remote Sensing*, San Francisco, California (1985).
38. H. Huo et al., "Mineral mapping and ore prospecting with HyMap data over eastern Tien Shan, Xinjiang Uyghur Autonomous Region," *Remote Sensing* **6**(12), 11829–11851 (2014).

39. R. N. Clark et al., "Imaging spectroscopy: earth and planetary remote sensing with the USGS tetracorder and expert systems," *J. Geophys. Res.* **108**(12), 5131–5135 (2003).
40. X. M. Huang and P. H. Hsu, "Comparison of wavelet-based and HHT-based feature extraction methods for Hyperspectral image classification," in *Int. Archives of the Photogrammetry, Remote Sensing and Spatial Information Sciences*, Vol. B7, pp. 121–126 (2012).

Jing Wei received his BE degree in remote sensing science and technology in 2014 and now is an undergraduate student in photogrammetry and remote sensing at Shandong University of Science and Technology. Currently, he is a junior research assistant at the Chinese University of Hong Kong. He is mainly focused on quantitative studies of optical and hyperspectral remote sensing.

Yanfang Ming received her MS degree in geology from Nanjing Normal University, specializing in paleoclimate analysis by studying the speleothem record. After receiving her PhD in geological remote sensing from Shandong University of Science and Technology, she focused on the identification of mineral types from hyperspectral remote sensing data. She is a lecturer at Shandong University of Science and Technology.

Qiang Jia received his PhD in geology from China University of Petroleum in 2012, specializing in sedimentology, stratigraphical paleontology, petrology, and mineralogy. He has been involved in teaching and researching in the College of Earth Science and Engineering at Shandong University of Science and Technology for more than 10 years. He is an expert in the field of microscopic analysis of sedimentary rock.

Dongxu Yang received his MSc degree in tourism management from the University of Birmingham in 2008 and now is teaching at Zhejiang Tourism College. Currently, he is the PhD candidate at the Central South University of Forestry and Technology. He mainly focused on tourism resources management.